

Inferred Linear Stability of Parker Solar Probe Observations using One- and Two-Component Proton Distributions

K.G. KLEIN,¹ J.L. VERNIERO,² B. ALTERMAN,³ S. BALE,^{4,2,5,6} A. CASE,⁷ J.C. KASPER,⁷ K. KORRECK,⁷ D. LARSON,²
E. LICHKO,¹ R. LIVI,² M. MCMANUS,² M. MARTINOVIĆ,¹ A. RAHMATI,² M. STEVENS,⁷ AND P. WHITTLESEY²

¹*University of Arizona, Tucson, AZ, USA*

²*Space Sciences Laboratory, University of California, Berkeley, CA 94720-7450, USA*

³*Space Science and Engineering, Southwest Research Institute, San Antonio, TX, USA*

⁴*Physics Department, University of California, Berkeley, CA 94720-7300, USA*

⁵*The Blackett Laboratory, Imperial College London, London, SW7 2AZ, UK*

⁶*School of Physics and Astronomy, Queen Mary University of London, London E1 4NS, UK*

⁷*Smithsonian Astrophysical Observatory, Cambridge, MA, USA*

ABSTRACT

The hot and diffuse nature of the Sun’s extended atmosphere allows it to persist in non-equilibrium states for long enough that wave-particle instabilities can arise and modify the evolution of the expanding solar wind. Determining which instabilities arise, and how significant a role they play in governing the dynamics of the solar wind, has been a decades-long process involving in situ observations at a variety of radial distances. With new measurements from Parker Solar Probe (PSP), we can study what wave modes are driven near the Sun, and calculate what instabilities are predicted for different models of the underlying particle populations. We model two hours-long intervals of PSP/SPAN-i measurements of the proton phase-space density during PSP’s fourth perihelion with the Sun using two commonly used descriptions for the underlying velocity distribution. The linear stability and growth rates associated with the two models are calculated and compared. We find that both selected intervals are susceptible to resonant instabilities, though the growth rates and kind of modes driven unstable vary depending on if the protons are modeled using one or two components. In some cases, the predicted growth rates are large enough to compete with other dynamic processes, such as the nonlinear turbulent transfer of energy, in contrast with relatively slower instabilities at larger radial distances from the Sun.

Keywords: solar wind — plasmas — instabilities — Sun: corona

1. INTRODUCTION

Wave-particle interactions are suspected of affecting the evolution of the solar wind as it is accelerated from the Sun’s surface and expands into the heliosphere; c.f. reviews in Matteini et al. (2012); Yoon (2017); Verscharen et al. (2019). Such instabilities are driven by departures from local thermodynamic equilibrium (LTE) that are frequently modeled using velocity distributions with anisotropic temperatures $T_{\perp,j}$ and $T_{\parallel,j}$ with respect to local magnetic field \mathbf{B} , relative field-aligned drifts between constituent plasma populations $\Delta v_{i,j} = (\mathbf{V}_i - \mathbf{V}_j) \cdot \mathbf{B}/|\mathbf{B}|$, and temperature disequilibrium between species $T_i \neq T_j$. The simultaneous effects of multiple sources of free energy can complicate a simple linear analysis; for instance, it has been found that the free energy contributions to unstable behavior from different ion and electron species can be non-negligible (Chen et al. 2016). To address this difficulty, previous

works have applied a numerical implementation of the Nyquist instability criterion (Nyquist 1932; Klein et al. 2017) to selected solar wind observations from the Wind (Klein et al. 2018) and Helios (Klein et al. 2019) missions, finding that a majority of intervals were unstable, including many intervals that simple parametric models accounting for a single source of free energy would have predicted to be stable.

Given the complexity of phase-space distributions typically found in weakly collisional plasmas, a number of different schemes for modeling the underlying velocity-space structure are frequently used; for instance, it is common to treat the protons as a single, anisotropic bi-Maxwellian or kappa distribution, or as a linear combination of core and relatively drifting beam distributions, each with distinct parallel and perpendicular temperatures; see the introduction of Alterman et al. (2018) for

a review of solar wind observations of secondary ion populations.

In this work, we select two hours-long time intervals observed by the SPAN-i instrument from the SWEAP instrument suite (Kasper et al. 2015) on Parker Solar Probe (PSP) (Fox et al. 2015) during its fourth encounter with the Sun, where significant ion-scale wave activity is observed, similar to activity previously reported in Bowen et al. (2020) and Verniero et al. (2020). We generate both a *one-component* and *two-component* model for each measurement of the proton velocity distribution, calculating and comparing the associated linear stability. Using the different models produces significantly different instabilities, either in the robustness of the associated growth rates or the kinds of waves driven unstable. The two-component model generally predicts ion-scale waves with characteristics more in line with the observed wave activity than models using a single proton component. This suggests that using overly simplistic models for ion distributions may neglect essential kinetic-scale processes responsible for the generation of these waves, even if these models capture macroscopic departures from LTE.

2. DATA AND METHODOLOGY

2.1. Parker Solar Probe Data

We select two hours-long sections from the outbound pass of PSP's fourth encounter with the Sun, when SPAN-i had sufficient coverage of the proton velocity distribution to model $f_p(\mathbf{v})$, specifically **Selection A: 2020/01/30 11:00-13:30** (SA, Fig. 1) and **Selection B: 2020/02/01 00:10-02:00** (SB, Fig. 2). During both selections, ion-scale electromagnetic waves are observed by the FIELDS instrument suite (Bale et al. 2016). Figs. 1 and 2 show the vector magnetic field components, as well as the trace power spectral density normalized to an ansatz power-law distribution for the background turbulent spectrum of $f^{-5/3}$, and the polarization of the transverse components of the magnetic fields, where red (blue) indicates right-handed (left-handed) circular polarization in the spacecraft frame. In SA, we see an abundance of power above a $f^{-5/3}$ spectrum persist for several hours near 3 Hz. At the same frequencies, we see a clear signature (red) of right-hand polarization persist for nearly the entire duration of the more than two-hour selection.

Unlike in SA, in SB there is not a persistent signature at a nearly constant frequency of ion-scale waves of a single handedness; both left-handed (blue) and right-handed (red) polarized waves are observed. There are also times during SB where no enhanced wave activity near ion frequencies is observed.

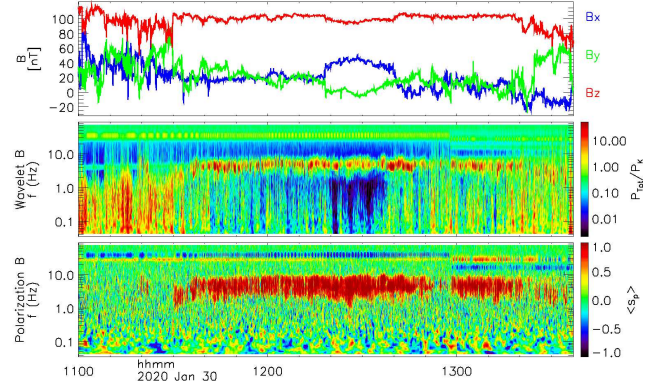


Figure 1. Magnetic field characteristics observed by FIELDS/PSP during Selection A, 2020/01/30 11:00-13:30. Top row: vector components of \mathbf{B} . Second row: Trace power spectral density normalized by $k^{-5/3}$ power law. Third row: Polarization of transverse magnetic field components, where red indicates right-handed circular polarization in the spacecraft frame.

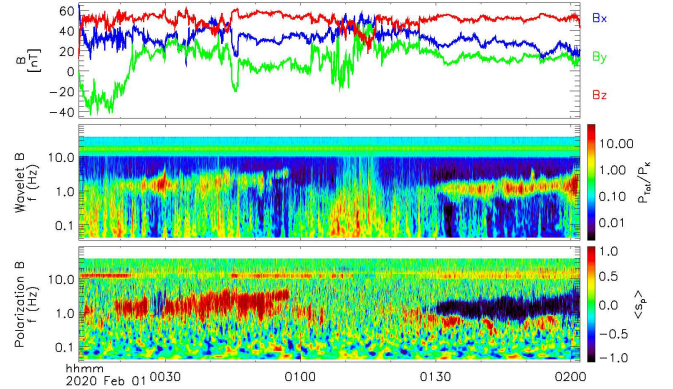


Figure 2. Magnetic field characteristics observed by FIELDS/PSP during Selection B, 2020/02/01 00:10-02:00, organized in the same fashion as Fig. 1.

2.2. One- and Two-Component Proton Distributions

For each ≈ 7 second measurement where a significant fraction of the thermal proton distribution is in the SPAN-i field of view, a two-component fit of the observed proton energy and angle spectra is attempted, modeling the protons as a combination of two relatively drifting bi-Maxwellian distributions,

$$f_p^{2\text{-comp.}}(v_{\perp}, v_{\parallel}) = \sum_{j=c,b} \frac{n_j}{\pi^{3/2} w_{\perp,j}^2 w_{\parallel,j}} \exp \left[-\frac{v_{\perp}^2}{w_{\perp,j}^2} - \frac{(v_{\parallel} - V_j)^2}{w_{\parallel,j}^2} \right]. \quad (1)$$

Parallel and perpendicular are defined with respect to the local mean-magnetic field direction, n_j is the component density, V_j the component bulk speed, and $w_{\perp,\parallel,j} = \sqrt{2T_{\perp,\parallel,j}/m_j}$ the component thermal velocities. This fit represents our *two-component model*. To mitigate

the partial FOV coverage of SPAN-i, all fitted densities were calibrated to QTN densities. All calculations using this model are performed in the proton center-of-mass frame.

For a model with the same macroscopic thermodynamic quantities, i.e. total proton density as well as parallel and perpendicular thermal pressures, that are used in a linear instability calculation that does not represent the beam-and-core structure of the protons observed in the inner heliosphere, we construct a *one-component model* as

$$f_p^{1\text{-comp.}}(v_\perp, v_\parallel) = \frac{n_p}{\pi^{3/2} w_{\perp,p}^2 w_{\parallel,p}} \exp \left[-\frac{v_\perp^2}{w_{\perp,p}^2} - \frac{v_\parallel^2}{w_{\parallel,p}^2} \right]. \quad (2)$$

Here, the proton density is $n_p = n_c + n_b$ and the total thermal velocities are $w_{\perp,\parallel,p} = \sqrt{2T_{\perp,\parallel,p}/m_p}$. We have defined the perpendicular proton temperature as

$$T_{\perp,p} = \frac{n_c T_{\perp,c} + n_b T_{\perp,b}}{n_c + n_b} \quad (3)$$

and the parallel proton temperature as

$$T_{\parallel,p} = \frac{n_c T_{\parallel,c} + n_b T_{\parallel,b} + \left(\frac{n_c n_b}{n_c + n_b} \right) m_p \Delta v_{cb}^2}{n_c + n_b}. \quad (4)$$

We emphasize that this is not equivalent to fitting the measured proton VDF with a single bi-Maxwellian distribution. Our method is employed so that both models have the same macroscopic perpendicular and parallel proton pressures, which would not necessarily be the case for a single bi-Maxwellian fit of protons with a significant secondary population.

The parameters from both models, along with measurements of the magnetic field strength averaged to the SPAN-i measurement cadence, are combined into the dimensionless parameters used as inputs for the Nyquist instability analysis. We will see that the significant differences in the underlying proton phase-space densities for the two models lead to significant differences in the predicted unstable behavior.

2.3. Instability Analysis

We employ a numerical implementation of the Nyquist instability criterion (Nyquist 1932; Klein et al. 2017) for the hot plasma dispersion relation for an arbitrary number of relatively drifting bi-Maxwellian components as determined by the PLUME numerical dispersion solver (Klein & Howes 2015). The Nyquist criterion determines the stability of a linear system of equations through a conformal mapping of the contour integral of a dispersion relation $\mathcal{D}(\omega, \mathbf{k}, \mathcal{P})$ over the upper-half

of the complex frequency plane. This integral counts the number of normal mode solutions that are unstable, having $\gamma > 0$, for a specific wavevector \mathbf{k} and set of dimensionless parameters \mathcal{P} ; ω_r and γ are the real and imaginary components of the complex frequency ω . Iterating this process for multiple contours with increasing values of γ enables the determination of the maximum growth rate and associated characteristics of the fastest growing mode supported by a particular \mathbf{k} . We have set $\gamma = 10^{-4} \Omega_p$ as the minimum growth rate for a wavevector to be considered unstable. We repeat this process over a log-spaced grid in wavevector space $k_\perp \rho_p \in [10^{-3}, 3]$ and $k_\parallel \rho_p \in [10^{-2}, 3]$, enabling the determination of the fastest growing mode for all wavevectors given a particular parameter set \mathcal{P} .

For the one-component model, the set of dimensionless plasma parameters is

$$\mathcal{P}_{1\text{-comp}} = \left(\beta_{\parallel,p}, \frac{w_{\parallel,p}}{c}, \frac{T_{\perp,p}}{T_{\parallel,p}} \right) \quad (5)$$

while for the two-component model, the dimensionless plasma parameters are

$$\mathcal{P}_{2\text{-comp}} = \left(\beta_{\parallel,c}, \frac{w_{\parallel,c}}{c}, \frac{T_{\perp,c}}{T_{\parallel,c}}, \frac{T_{\perp,b}}{T_{\parallel,b}}, \frac{n_b}{n_c}, \frac{T_{\perp,b}}{T_{\parallel,c}}, \frac{\Delta v_{b,c}}{v_{Ac}} \right), \quad (6)$$

where we define the thermal-to-magnetic pressure ratio $\beta_{\parallel,j} = 8\pi n_j T_{\parallel,j} / B^2$, the core-proton Alfvén velocity as $v_{Ac} = B / \sqrt{4\pi m_p n_c}$, and the speed of light c . Frequencies are normalized to the proton gyrofrequency $\Omega_p = q_p B / m_p c$. For this study, we neglect the contribution of alphas and other minor ions and treat the electrons as a single isotropic distribution with density and velocity necessary to enforce quasi-neutrality and zero net current. The impact of the non-proton components on stability will be the focus of future study.

Given an example SPAN-i measurement of $f_p(\mathbf{v})$, shown in Fig. 3, both the one-component and two-component models are constructed, producing the sets of dimensionless parameters $\mathcal{P}_{1\text{-comp}}$ and $\mathcal{P}_{2\text{-comp}}$. For the selected example, starting at 11:16:22 on 01/30/2020, these sets are:

$$\mathcal{P}_{1\text{-comp}} = \left(\beta_{\parallel,p} = 1.0646, \frac{w_{\parallel,p}}{c} = 2.786 \times 10^{-4}, \frac{T_{\perp,p}}{T_{\parallel,p}} = 0.389 \right) \quad (7)$$

and

$$\mathcal{P}_{2\text{-comp}} = \left(\beta_{\parallel,c} = 0.410, \frac{w_{\parallel,c}}{c} = 1.861 \times 10^{-4}, \frac{T_{\perp,c}}{T_{\parallel,c}} = 0.770, \frac{T_{\perp,b}}{T_{\parallel,b}} = 0.620, \frac{n_b}{n_c} = 0.157, \frac{T_{\perp,b}}{T_{\parallel,c}} = 2.465, \frac{\Delta v_{b,c}}{v_{Ac}} = -1.350 \right). \quad (8)$$

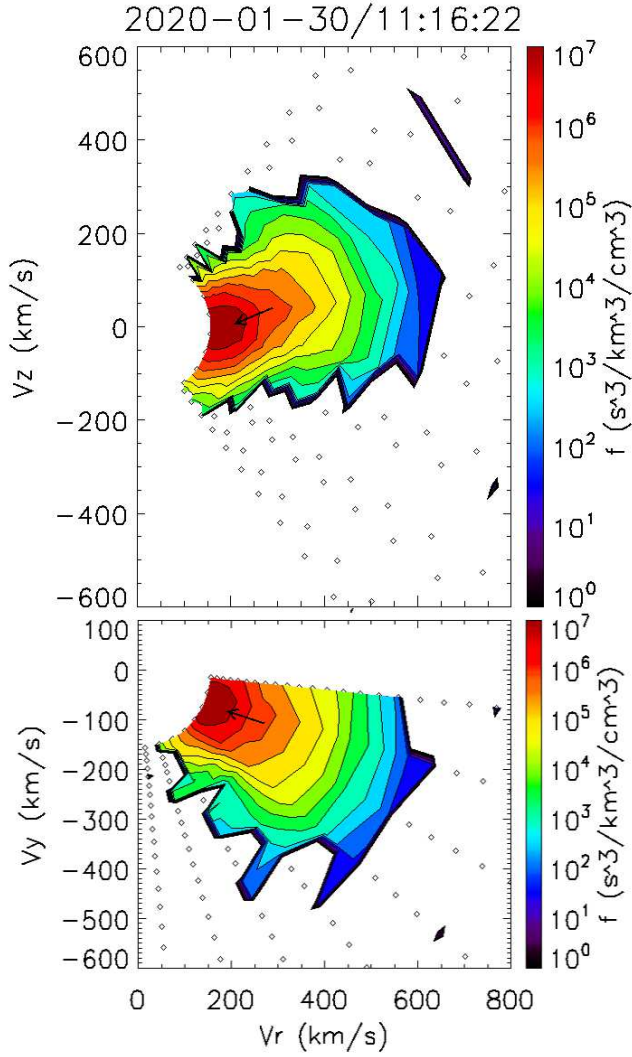


Figure 3. SPAN-i observation of the proton velocity distribution for the interval under analysis in Fig. 4 as a function of v_z and v_r (top) and v_y and v_r (bottom), in SPAN-i instrument coordinates where $v_r = \sqrt{v_x^2 + v_y^2}$. Diamonds represent the central values of the instrument’s velocity space bins, color the proton distribution phase-space density, and the arrow magnetic field orientation with the length representing the Alfvén speed.

Given these sets, we calculated $\gamma^{\max}(\mathbf{k}d_p)/\Omega_p$ using the Nyquist method, shown in the top two panels in Fig. 4, which in turn allows the calculation of γ^{\max}/Ω_p over the entire wavevector range, as well as the associated ω_r^{\max}/Ω_p , $k^{\max}d_p$, θ_{kB}^{\max} , and other eigenfunctions of the unstable modes. For this measurement and associated models, γ^{\max}/Ω_p is significantly larger for the two-component model and the wavevector region supporting unstable modes is broader compared to the one-component model, though both models predict

the same mode, the parallel propagating firehose/fast-magnetosonic wave, to be linearly unstable.

For validation, we compare these predicted properties to the normal mode solutions for the forward and backward parallel propagating Alfvén and fast-magnetosonic waves numerically calculated using the PLUME dispersion solver (Klein & Howes 2015). The central rows of Fig. 4 show the real component of the normal mode frequency $\omega_r(k_{\parallel}d_p)/\Omega_p$ for fixed $k_{\perp}d_p = 10^{-3}$, the normalized growth or damping rates $\gamma(k_{\parallel}d_p)/|\omega_r|$, and the normalized $n = \pm 1$ cyclotron resonant velocities,

$$\frac{v_{\text{res}}(k_{\parallel})}{v_A} = \frac{\omega_r(k_{\parallel}) - n\Omega_p}{k_{\parallel}v_A} \quad (9)$$

where the choice of sign of n is determined by the wave’s polarization and direction of propagation; $n = +1$ for the forward Alfvén and backwards fast modes and $n = -1$ for the backwards Alfvén and forward fast modes. For these nearly parallel modes, there is no significant $n = 0$ contribution to the wave-particle interaction. We find good agreement with the kinds of modes and region of wavevectors predicted to be stable and unstable from both the Nyquist and traditional dispersion calculation.

Both models are unstable to the parallel firehose instability for this interval, but there are significant differences—illustrated in the bottom panels of Fig. 4—in the resonant coupling between the protons and the electric field. The wave-phase velocity for each of the four parallel propagating modes at a fixed wavevector $k_{\parallel}d_p$, set to be $|k^{\max}|d_p$ for the one- or two-component model, is illustrated as a dashed vertical line compared to the model phase-space density $f_p(v_{\perp}/v_A, v_{\parallel}/v_A)$. The $n = \pm 1$ cyclotron resonant velocity is shown as a solid vertical line, and contours of constant energy in the wave-frame are illustrated as colored half-circles. The sign of the pitch angle gradient of f_p where the resonant velocity meets the contours of constant energy determines if energy is transferred from the wave to the protons, leading to damping of the wave, or from the protons to the wave, leading to excitation and instability. For this interval, the fitting of a secondary proton population leads to the suppression of the unstable anti-beam-aligned fast mode and the enhancement of the beam-aligned fast mode’s growth rate. The beam component also significantly increases the damping rate of the anti-beam aligned Alfvén mode, leading it to switch propagation directions at $k_{\parallel}d_p \approx 0.3$.

3. INFERRED STABILITY ACROSS SELECTIONS

The Nyquist instability analysis described in §2.3 is performed over the entirety of SA, Fig. 5, and SB, Fig. 6,

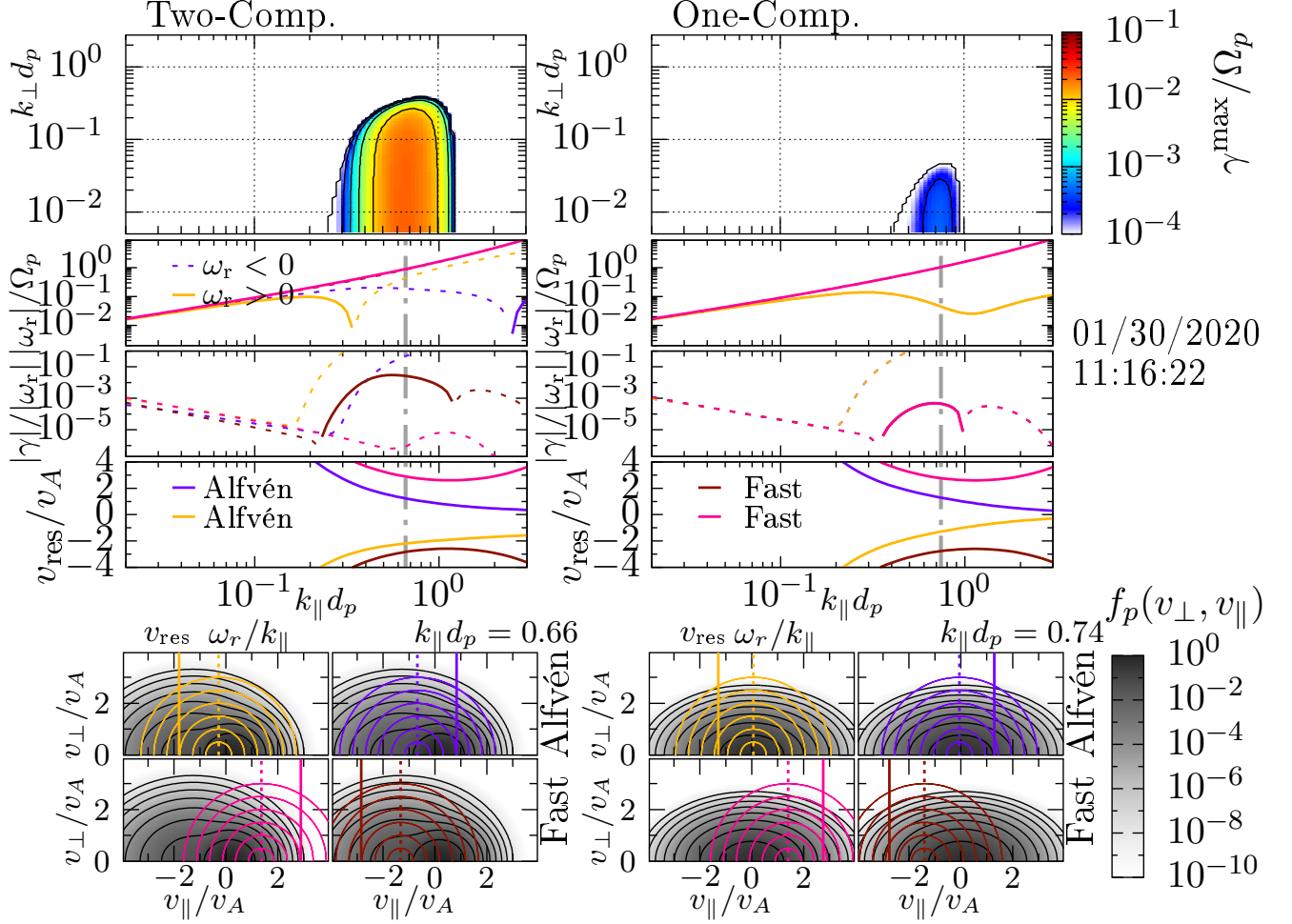


Figure 4. Comparison of linear stability and resonances for the one- and two-component models, left and right columns, associated with the SPANi observation shown in Fig. 3. Top row: Fastest growing mode calculated by the Nyquist method as a function of $k_{\perp} d_p$ and $k_{\parallel} d_p$. Second row: linear dispersion relation $\omega_r(k_{\parallel} d_p)/\Omega_p$ for the four weakly damped, parallel propagating linear modes. Third: Normalized growth (solid) or damping (dashed) rates γ/ω_r for the same modes. Fourth: Cyclotron resonant velocities normalized to v_A . Bottom: Illustration of phase (dashed vertical) and resonant (solid) velocities for the four modes at the wavevector associated with the maximum growth rate (dot-dashed line in middle panels), the associated curves of constant energy in the wave-frame, and the phase-space densities associated with the one- and two-component models (grey-scale).

for both the one- and two-component models (red and blue).

For both selections, we see different predicted unstable behavior for the two models. Using the one-component model for SA, only 40.5% of the intervals are found to be unstable, and of those most have relatively weak growth rates, with a median value of $\bar{\gamma}_{1-\text{comp}}^{\text{max}} = 2.33_{1.57}^{3.41} \times 10^{-4} \Omega_p$. The sub- and super-scripts represent the 25th and 75th percentiles of the unstable mode growth rate distribution. These are parallel firehose instabilities, where sufficiently extreme parallel-to-perpendicular thermal pressure ratios, manifest in a one-component proton distribution, change the sign of the velocity gradient at the cyclotron resonant velocity such that energy is extracted from the protons to drive an unstable fast-magnetosonic mode. Due to the symmetry of

the one-component model, both forward and backward propagating modes are driven. No other kinds of unstable modes are supported by the one-component model during SA.

For the two-component model, 99.9% of the intervals in SA are found to be unstable, with a median growth rate of $\bar{\gamma}_{2-\text{comp}}^{\text{max}} = 2.54_{1.92}^{3.24} \times 10^{-2} \Omega_p$, two orders of magnitude larger than for the one component model. All of the unstable intervals are associated with parallel propagating fast-magnetosonic modes with $|k|_{\text{max}}^{\text{max}} d_p \approx 0.5$. Unlike the symmetrically emitted unstable waves from the one-component model, the unstable modes from the two-component model only propagate in the same di-

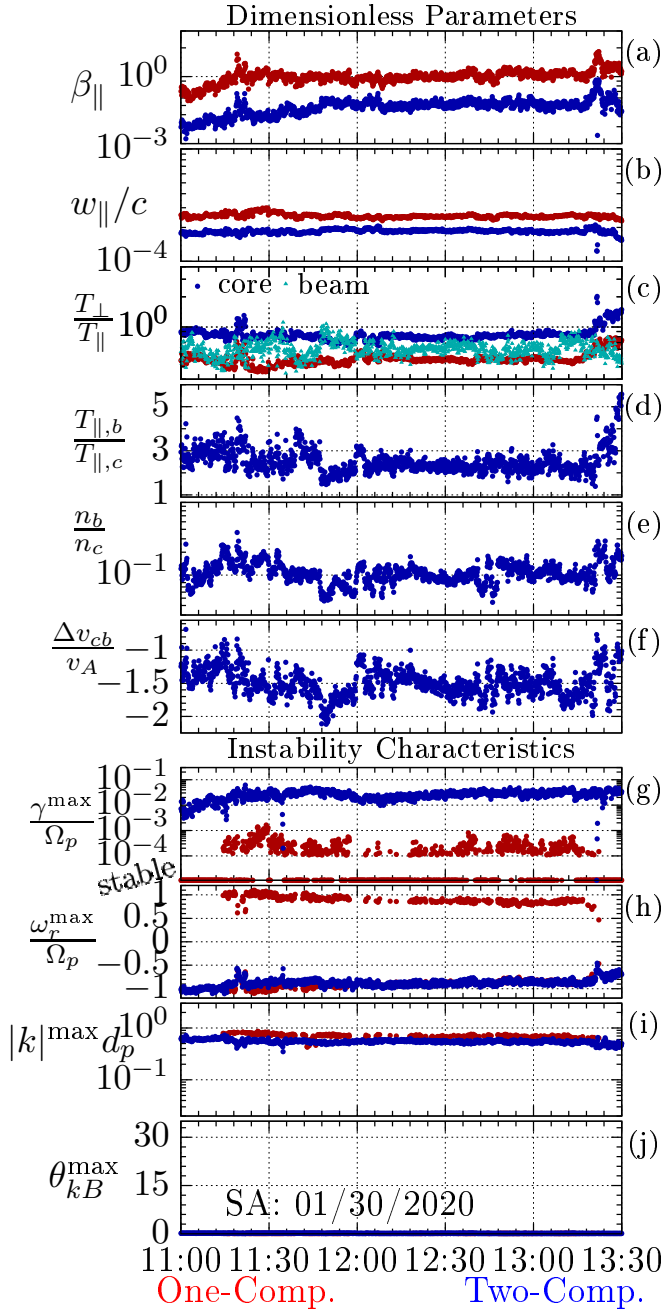


Figure 5. Dimensionless parameters from one- and two-component (red and blue) models for SA, (a-f) and calculated instability characteristics, (g-j). (a): thermal-to-magnetic pressure ratio $\beta_{\parallel,p}$ or $\beta_{\parallel,c}$, (b): thermal-speed ratio $w_{\parallel,p}/c$ or $w_{\parallel,c}/c$, (c): temperature anisotropy $T_{\perp,p}/T_{\parallel,p}$ or $T_{\perp,c}/T_{\parallel,c}$ ($T_{\perp,b}/T_{\parallel,b}$ in teal), (d): temperature disequilibrium $T_{\parallel,b}/T_{\parallel,c}$, (e): density ratio n_b/n_c , (f): relative drift velocity $\Delta v_{bc}/v_A$. (g): maximum growth rate γ^{\max}/Ω_p (h): normal mode real frequency ω_r^{\max}/Ω_p (i & j): Amplitude and angle, $|k|^{\max} d_p$ and θ_{kB}^{\max} of the wavevector associated with fastest growing mode.

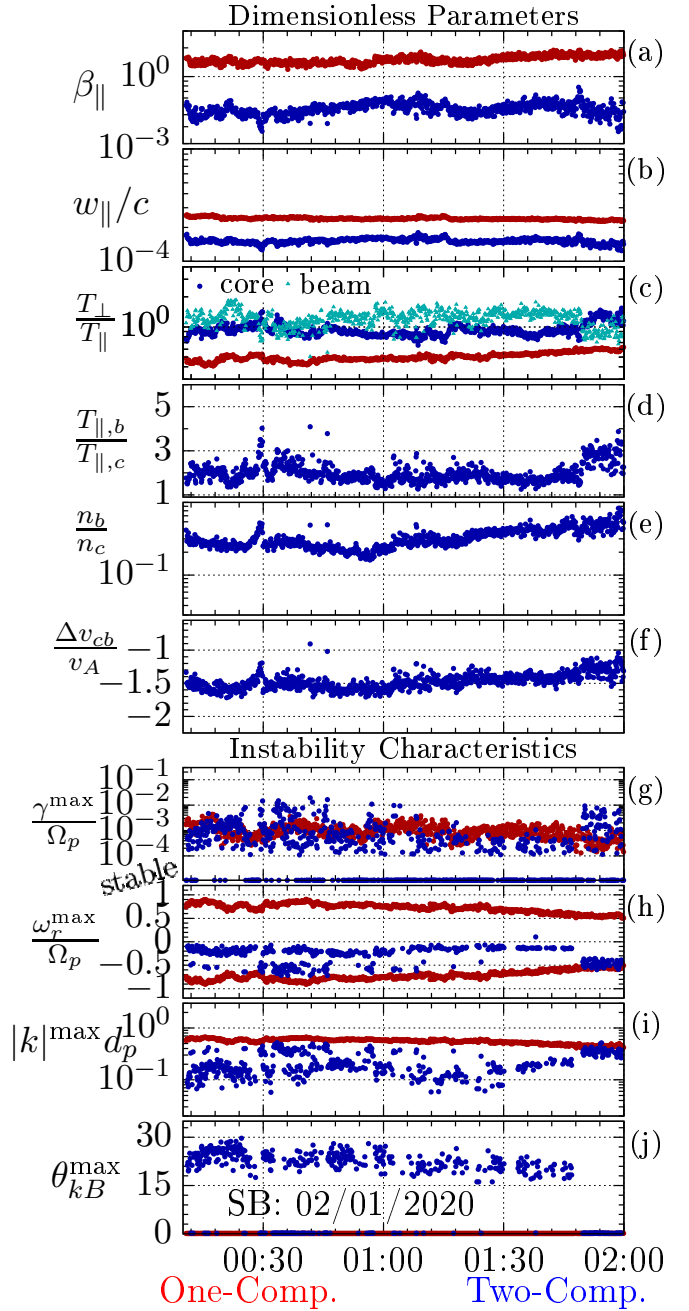


Figure 6. Dimensionless parameters and calculated instability characteristics from one- and two-component (red and blue) models for SB organized in the same format as Fig. 5.

rection as the secondary proton population.¹ The maxi-

¹ We define the radial component of our coordinate system to align with the mean magnetic field. In both SA and SB, PSP was in a region of Sunward magnetic polarity, meaning that the anti-Sunward propagating secondary proton populations have a negative velocity with respect to the primary proton population.

imum growth rate of the unstable fast mode is enhanced due to an increased phase-space density associated with the secondary proton population, while the anti-beam aligned fast-mode resonance is effectively starved of protons with which to interact, leading to damping rather than instability for this mode.

We find differences in the kinds of instabilities predicted for the two models in SB. Ninety-nine percent of the intervals are predicted to be linearly unstable to the parallel propagating firehose instability for the one-component model, with a median growth rate of $\bar{\gamma}_{1\text{-comp}}^{\max} = 9.26_{6.12}^{13.3} \times 10^{-4} \Omega_p$. This is *not* the case for the two-component model. The median growth rate for the two-component model is similar, $\bar{\gamma}_{2\text{-comp}}^{\max} = 6.43_{3.30}^{15.6} \times 10^{-4} \Omega_p$, however only 55.7% of the intervals are found to be unstable and the associated fastest growing mode oscillates between a beam-aligned, parallel propagating firehose mode and an oblique instability. This demonstrates that fitting a secondary component does not universally enhance the predicted growth rate and that more sophisticated treatments of velocity-space structure can lead to the generation of different kinds of unstable modes.

As seen in Fig. 7, γ^{\max}/Ω_p is generally larger for the two-component model than for the one-component model for SA. This is not the case for SB, where more of the one-component intervals are unstable, while the variance in the growth rate for the two-component model is larger. When re-normalized to the normal mode frequency ω_r^{\max} , Fig 7b, we see an enhancement in the growth rates for the two-component model in SB, while the other growth rates remain relatively unaffected.

Other time scales of potential interest include an estimate for the non-linear cascade rate at the wavevector of fastest growth,

$$\begin{aligned} \gamma^{\max} \tau_{nl} &= \left(\frac{\gamma^{\max}}{v_A} \right) (k_{\text{break}})^{-1/3} (|\mathbf{k}^{\max}|)^{-2/3} \quad (10) \\ &= \left(\frac{\gamma^{\max}}{\Omega_p} \right) \left(\frac{2\pi f_{\text{break}}}{\Omega_p} \frac{v_A}{v_{sw}} \right)^{-1/3} (|\mathbf{k}^{\max} d_p|)^{-2/3} \end{aligned}$$

where we approximate the transition from the injection to the inertial ranges of turbulence as $k_{\text{break}} = 2\pi f_{\text{break}}/v_{sw}$ with f_{break} found to be approximately 10^{-3} Hz when constructing trace power-spectral density curves for either SA or SB, not shown. These values are in rough agreement with the results reported in Chen et al. (2020). The cascade time is estimated as the critically balanced nonlinear cascade rate, $\tau_{nl} \sim \omega_{\text{Alfvén}}^{-1}$ (Goldreich & Sridhar 1995; Mallet et al. 2015). Previous analysis between 0.3 and 0.7 au (Klein et al. 2019) found that γ^{\max} never exceeded the estimated nonlinear cascade rate, though the two rates were found to be within an order of magnitude, with 50% of the

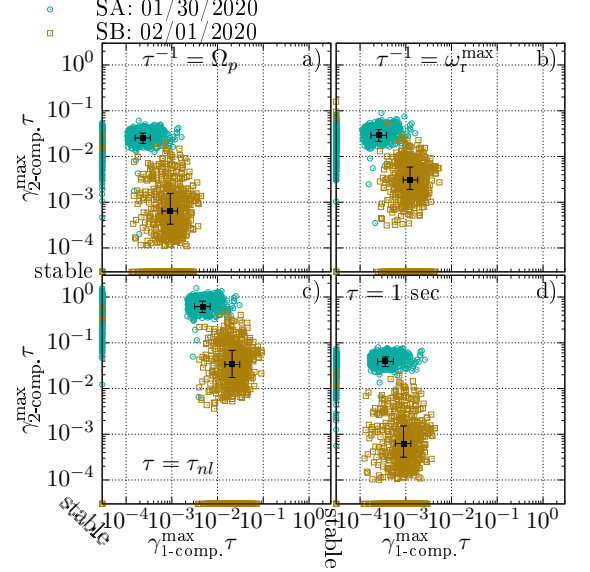


Figure 7. Comparison of normalized growth rates for the two models for SA (teal) and SB (gold), with the abscissa and ordinate mapping the one- and two-component rates. In panels a,b,c, and d, γ^{\max} is normalized to Ω_p , ω_r^{\max} , τ_{nl}^{-1} and 1 Hz respectively. Black dots and bars correspond to medians and 25th and 75th percentiles associated with the unstable intervals.

intervals having $\gamma^{\max} \tau_{nl} \gtrsim 0.2$. For the two-component model in SA, the maximum growth rate is of the same order as τ_{nl}^{-1} , with a median value of $\bar{\gamma}_{2\text{-comp}}^{\max} \tau_{nl} = 0.618_{0.463}^{0.813}$, indicating that these predicted instabilities operate on similar timescales as the nonlinear transport of energy through these spatial scales. Importantly, while $\bar{\gamma}_{2\text{-comp}}^{\max} \sim \tau_{nl}^{-1}$, the median value of $\bar{\gamma}_{1\text{-comp}}^{\max} \tau_{nl}$ is $4.70_{3.14}^{6.90} \times 10^{-3}$ for the same interval. This emphasizes that our choice of different models for the proton phase-space density will lead to drastically different interpretations of the importance of different physical processes. The impact of these instabilities, especially when the ions are modeled as multiple components, on the turbulent transport of energy must be considered in future modeling efforts. The median values of $\gamma^{\max} \tau_{nl}$ are comparable for SB, with $\bar{\gamma}_{1\text{-comp}}^{\max} \tau_{nl} = 2.08_{1.45}^{3.04} \times 10^{-2}$ and $\bar{\gamma}_{2\text{-comp}}^{\max} \tau_{nl} = 3.55_{1.74}^{6.81} \times 10^{-2}$, again showing that the two-component model does not universally enhance growth rates compared to the one-component model. To remove variations associated with the normalization by Ω_p due to changes in $|\mathbf{B}|$ as a function of time, we also plot the growth rate in Hertz, Fig 7d, and see a distribution of growth rates similar to that seen in panel a.

By design, the one- and two-component models have the same parallel and perpendicular thermal pressures for a given interval, which can be characterized by the

firehose (Kunz et al. 2015)

$$\Lambda_F = \frac{\beta_{\parallel} - \beta_{\perp}}{2} + \frac{\sum_j n_j m_j |\Delta \tilde{v}_j|^2}{\sum_j (n_j m_j) v_A^2} \quad (11)$$

or mirror (Hellinger 2007)

$$\Lambda_M = \sum_j \beta_{\perp,j} \left(\frac{\beta_{\perp,j}}{\beta_{\parallel,j}} - 1 \right) - \frac{\left(\sum_j q_j n_j \frac{\beta_{\perp,j}}{\beta_{\parallel,j}} \right)^2}{2 \sum_j \frac{(q_j n_j)^2}{\beta_{\parallel,j}}} \quad (12)$$

criterion, where $\Delta \tilde{v}_j$ is the difference between the bulk speed of component j and the center of mass velocity. When these criterion exceed unity, large-scale firehose or mirror instabilities are generated. For both SA and SB, the amplitude of neither criteria exceeds ~ 0.5 for either model; therefore, it is the resonances between the proton distribution and the associated electromagnetic fields and not the excess macroscopic parallel or perpendicular pressures that drives the predicted unstable wave modes.

Slight changes in the relative drift speed between the two proton populations and their densities can have a significant impact on the kind of unstable mode predicted to be generated. This is illustrated in Fig. 8, where nine sequential illustrations of contours of constant $\gamma^{\max}(\mathbf{k})$ are shown for the one- and two-component models for SPAN-i observations from near the beginning of SB. Throughout these two minutes both the maximum growth rates and regions of unstable wavevectors are largely unchanged for the one-component model. This is expected given that $T_{\perp,p}/T_{\parallel,p}$ and $\beta_{\parallel,p}$ are relatively constant over this time, remaining consistent with a parallel propagating firehose instability. For the two-component model, oblique modes are initially driven. A minute into the sequence, the maximum growth rate transitions to a parallel propagating wavevector, and then transitions back to an oblique instability. These transitions correspond to a temporary dip in the relative density of the beam component and an increase in the relative drift speed. Given that many kinds of waves are observed in this section of data, it appears plausible that these transitions between parallel and oblique instabilities may be real, but are not properly accounted for in overly simplistic models of the protons as a single anisotropic distribution, which only drive one kind of unstable mode.

We note that there is not a simple parametric function dependence only on n_b/n_c and $\Delta v_{b,c}/v_A$ that divides the parallel unstable modes from the oblique modes. In Fig. 9, we plot the angle of the fastest growing mode θ_{kB}^{\max} for the two-component model for SB as a function of these two parameters. Generally, the larger the rela-

tive drift, the more likely the model is predicted to generate an oblique unstable mode, with the transition between parallel and oblique modes arising at lower drifts for larger relative beam densities. However, we find many stable intervals with very similar drifts and densities to the intervals unstable to the generation of both parallel and oblique unstable modes. This can be understood by recalling that the variation of the temperatures and anisotropies of the individual proton components will have a significant impact on the predicted stability of the system that is not captured in this reduced parameter space. Due to this complexity, we do not attempt to offer a simple parametric prescription for this transition between parallel and oblique instabilities in this work, but do note again that if this distribution is treated as a single proton population, the only instability supported is the parallel-propagating, fast/magnetosonic firehose instability.

4. CONCLUSIONS

In this work, we have selected two hours-long intervals where in situ measurements of the local plasma conditions have been made during PSP's fourth perihelion orbit. These measurements coincide with significant ion-scale wave activity as observed by the FIELDS magnetometers. The proton phase-space densities have been modeled as either a single anisotropic population, or two relatively drifting anisotropic populations. The linear stability of both models was calculated, with strikingly different predictions for the supported linear modes. In the first selection, both models produce the same kind of unstable mode, but the two-component model drives instabilities that grow nearly two orders of magnitude faster, fast enough to potentially act on the same timescales as the local nonlinear turbulent transfer of energy. Additionally, the two-component model for SA only drives instabilities propagating in a single direction, as opposed to the one-component model where waves are driven both Sunward and anti-Sunward due to the enforced symmetry of the simplified description of the protons. For the second selection, modeling the protons using two components does not make the plasma more unstable, but does change the kind of unstable modes driven, leading to an oscillation between the production of parallel and oblique propagating waves.

As future lines of inquiry, we intend on extending this work to investigate the predicted growth rates and waves concurrently observed with other plasma parameters and solar wind conditions, such as intervals where the total parallel proton pressure is exceeded by the total perpendicular pressure. We will also include additional sources of free energy associated with minor

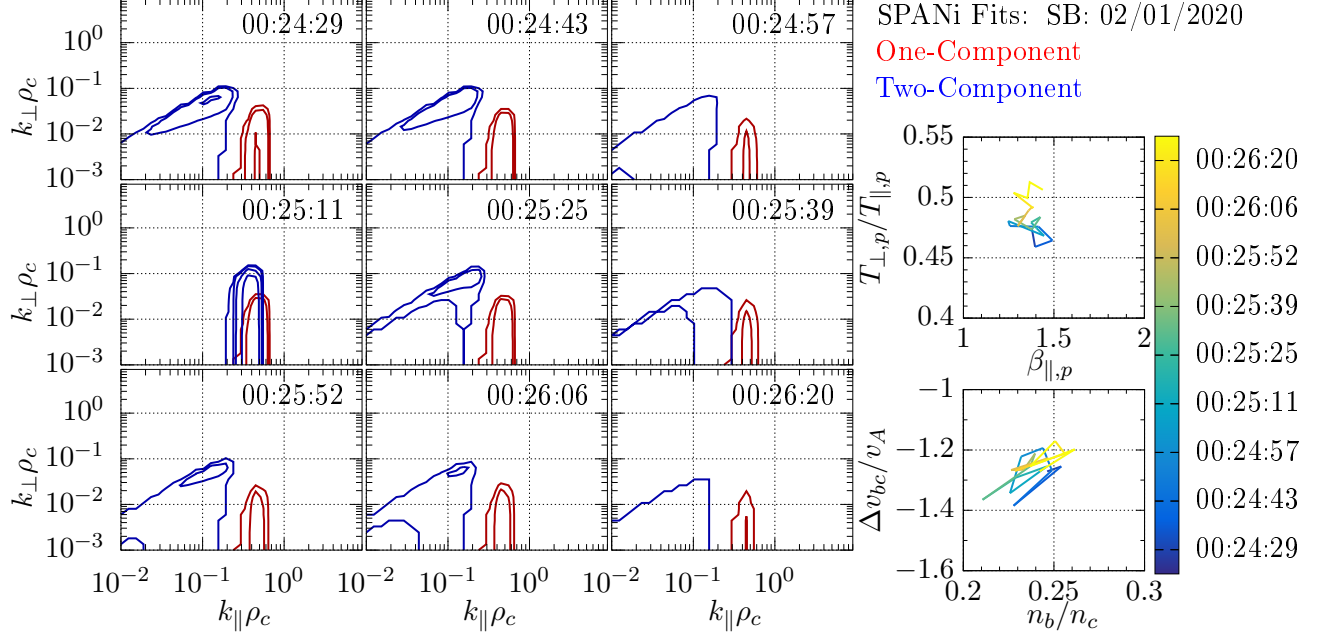


Figure 8. Left: Contours of constant γ^{\max}/Ω_p as a function of $k_{\perp}\rho_c$ and $k_{\parallel}\rho_c$ for the one- and two-component models (red and blue) for nine intervals at the start of SB. Right: Temporal variation of $T_{\perp,p}/T_{\parallel,p}$ and $\beta_{\parallel,p}$ from the one-component model (top) and of the relative drifts and densities of the two-component model (bottom).

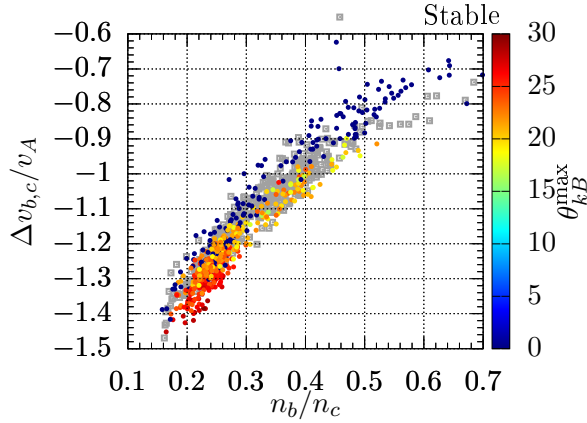


Figure 9. Wavevector angle θ_{kB}^{\max} of fastest growing mode during SB calculated using the two-component model, indicated by color, as a function of relative densities n_b/n_c and drift velocities $\Delta v_{bc}/v_A$. Grey squares indicate intervals predicted to be linearly stable.

ions and electrons, to determine if they act to enhance or stabilize these growing modes. This work will help to ascertain under what conditions which models may suffice to properly describe kinetic processes. Importantly, as the instabilities under consideration are resonant, we must also consider the impact of departures from bi-Maxwellian distributions, either using other analytic prescriptions, e.g. kappa (Livadiotis 2015) or flat-top distributions (Klein & Chandran 2016; Wilson et al. 2020), or via a direct numerical integration of the observed phase-space density (Verscharen et al. 2018).

The SWEAP Investigation and this publication are supported by the PSP mission under NASA contract NNN06AA01C. K.G.K. is supported by NASA ECIP Grant 80NSSC19K0912. An allocation of computer time from the UA Research Computing High Performance Computing at the University of Arizona is gratefully acknowledged.

REFERENCES

- Alterman, B. L., Kasper, J. C., Stevens, M. L., & Koval, A. 2018, *Astrophys. J.*, 864, 112
- Bale, S. D., Goetz, K., Harvey, P. R., et al. 2016, *Space Sci. Rev.*, doi:10.1007/s11214-016-0244-5
- Bowen, T. A., Mallet, A., Huang, J., et al. 2020, *Astrophys. J. Supp.*, 246, 66
- Chen, C. H. K., Matteini, L., Schekochihin, A. A., et al. 2016, *Astrophys. J. Lett.*, 825, L26
- Chen, C. H. K., Bale, S. D., Bonnell, J. W., et al. 2020, *Astrophys. J. Supp.*, 246, 53
- Fox, N. J., Velli, M. C., Bale, S. D., et al. 2015, *Space Sci. Rev.*, doi:10.1007/s11214-015-0211-6

- Goldreich, P., & Sridhar, S. 1995, *Astrophys. J.*, 438, 763
- Hellinger, P. 2007, *Phys. Plasmas*, 14, 082105
- Kasper, J. C., Abiad, R., Austin, G., et al. 2015, *Space Sci. Rev.*, 1
- Klein, K. G., Alterman, B. L., Stevens, M. L., Vech, D., & Kasper, J. C. 2018, *Phys. Rev. Lett.*, 120, 205102
- Klein, K. G., & Chandran, B. D. G. 2016, *Astrophys. J.*, 820, 47
- Klein, K. G., & Howes, G. G. 2015, *Phys. Plasmas*, 22, 032903
- Klein, K. G., Kasper, J. C., Korreck, K. E., & Stevens, M. L. 2017, *Journal of Geophysical Research (Space Physics)*, 122, 9815
- Klein, K. G., Martinović, M., Stansby, D., & Horbury, T. S. 2019, *Astrophys. J.*, 887, 234
- Kunz, M. W., Schekochihin, A. A., Chen, C. H. K., Abel, I. G., & Cowley, S. C. 2015, *Journal of Plasma Physics*, 81, 325810501
- Livadiotis, G. 2015, *Journal of Geophysical Research (Space Physics)*, 120, 1607
- Mallet, A., Schekochihin, A. A., & Chandran, B. D. G. 2015, *Mon. Not. Roy. Astron. Soc.*, 449, L77
- Matteini, L., Hellinger, P., Landi, S., Trávníček, P. M., & Velli, M. 2012, *Space Sci. Rev.*, 172, 373
- Nyquist, H. 1932, *Bell system technical journal*, 11, 126
- Verniero, J. L., Larson, D. E., Livi, R., et al. 2020, *Astrophys. J. Supp.*, 248, 5
- Verscharen, D., Klein, K. G., Chandran, B. D. G., et al. 2018, *Journal of Plasma Physics*, 84, 905840403
- Verscharen, D., Klein, K. G., & Maruca, B. A. 2019, *Living Rev. Solar Phys.*, 16, 5
- Wilson, Lynn B., I., Chen, L.-J., Wang, S., et al. 2020, *Astrophys. J.*, 893, 22
- Yoon, P. H. 2017, *Reviews of Modern Plasma Physics*, 1, 4